energies

MDPI

Article

Measurements of Soot Particulate Emissions of Ammonia-Ethylene Flames Using Laser Extinction Method

Cheng Tung Chong [1,*], Mingkun Cao [1], Bo Tian [2] and Tian Xie [1]

[1] China-UK Low Carbon College, Shanghai Jiao Tong University, Lingang, Shanghai 201306, China
[2] Department of Engineering, University of Leicester, Leicester LE1 7RH, UK; bt156@leicester.ac.uk
* Correspondence: ctchong@sjtu.edu.cn

Abstract: Ammonia (NH_3) has emerged as an attractive carbonless fuel that can be co-fired with hydrocarbon fuel to reduce carbon dioxide emissions. To understand the influence of NH_3 on soot formation when co-fired with hydrocarbons, the soot formation propensity is experimentally investigated via a laminar diffusion jet flame. A stable ethylene (C_2H_4) jet flame doped with NH_3 at different volume percentages was established for the investigation of soot formation tendency. OH* chemiluminescence imaging revealed the change of flame structure, in which the signals emitted from the heat release region weakened with increasing NH_3 addition, while the peak intensity shifted from the flame wings towards flame centerline region. The laser extinction method used to measure the soot volume fraction (SVF) at different heights above the burner, which showed the effect of NH_3 on soot suppression is significant, owing to the interaction between N-containing compounds with carbon atoms that result in the reduction of key intermediate products required for the formation of benzene and polycyclic aromatic hydrocarbons (PAH). The effect of soot inhibition appears to be stronger for the low NH_3 blend fraction. The chemistry effect of NH_3 on soot reduction for C_2H_4 flame is ascertained by comparing with N_2-doped C_2H_4 flame at the same volume percentage. This work highlights the need for improved understanding of hydrocarbon fuel with NH_3 to enable detailed understanding on the soot generation and oxidation process.

Keywords: ammonia; diffusion jet flame; laser extinction method; soot formation; soot volume fraction

Citation: Chong, C.T.; Cao, M.; Tian, B.; Xie, T. Measurements of Soot Particulate Emissions of Ammonia-Ethylene Flames Using Laser Extinction Method. *Energies* **2022**, *15*, 5209. https://doi.org/10.3390/en15145209

Academic Editor: Adonios Karpetis

Received: 25 May 2022
Accepted: 6 July 2022
Published: 18 July 2022

1. Introduction

The urgency to develop clean and sustainable energy solutions has been highlighted in the 26th United Nations Climate Change Conference of the Parties (COP26) to curb the rise of global temperature to within 2 °C [1]. Decarbonization of the energy sector is seen as one of the pertinent measures to achieve the carbon neutrality goal. As such, hydrogen produced from renewable energy sources has been identified as a key energy carrier that can replace the fossil-based hydrocarbon fuels [2]. The inherent high energy per unit mass for hydrogen and the absence of CO_2 emissions during combustion is hugely advantageous, making it a favorable alternative fuel. However, the issues of storage and safety concerning hydrogen usage present challenges for the deployment in the transportation sector [3]. Another carbon-neutral fuel that has recently gained significant attention is ammonia. The carbonless nitrogen-based fuel requires a moderate condition for fuel storage and transport and can be used in land-based power generation and low- and medium-speed engine operations [4]. However, some issues related to the ammonia's burning characteristics, such as low velocity and heating value, longer ignition delay time, and high NO_x emissions, need to be addressed when used as fuel in existing engines [5]. One way to overcome the drawbacks of ammonia is by adopting the co-firing strategy with hydrocarbon or hydrogen fuels.

The usage of ammonia as operating fuel requires detailed study on the emissions characteristics to enable the formulation of suitable strategy to minimize pollutant emissions.

Various studies regarding the combustion properties of NH_3 co-fired with a wide range of hydrocarbons have been documented in different reviews [6,7], including laminar flame speed, ignition delay, spray flame, chemical kinetics and emissions measurements, among others. Some researchers have extended the application of NH_3 in practical combustion devices such as internal combustion engine and micro gas turbine to examine the fuel's performances [4,5]. At present, oxidation studies of NH_3 have mainly focused on the emissions of gaseous pollutant, i.e., nitrous oxide (NO_x), owing to the detrimental impacts to human health and the strict industrial regulation of NO_x emission. Another pollutant that is equally harmful but less studied is the emissions of particulate matters, i.e., soot. The study of soot particles is of importance as the emissions of PAH, which is the soot precursor, is carcinogenic in nature, while the fine particulates of $PM_{2.5}$ are harmful to the respiratory system. To mitigate the effects of soot, the energy and transportation sectors have imposed stringent regulations on the emissions. The diesel fuel of EURO 6 standard specifies the limits of the number densities and mass of particulate matters [8]. The International Civil Aviation Organization (ICAO) implements the CAEP/8 (Committee on Aviation Environmental Protection/8) standard that limits the particulate matters emissions from aviation engine [9]. The International Maritime Organization (IMO) has specified the limit of particulate matter emissions for marine vessels via Regulation 14 [10]. These challenges have motivated the formulation of mitigation strategies and combustion techniques to reduce the soot emissions during combustion processes. Therefore, when considering the use of carbonless alternative fuel, the formation mechanism of soot and PAH needs to be elucidated to optimize the combustion process for minimum soot emissions.

Of late, some research groups have attempted to understand the fundamental sooting characteristics of ammonia co-fired with fossil hydrocarbon fuels. Li et al. [11] evaluated the influence of ethanol and ammonia addition on PAH formation in premixed ethylene flames. It was found that both ethanol and ammonia addition could cause PAH reductions in premixed ethylene flames as their blending ratios increase. The suppression of PAH was due to low concentration of key intermediates such as C_2H_2, C_3H_3, PC_3H_4, and C_4H_4 in flame, which are essential species needed for the formation of aromatic benzene ring and PAH growth [12]. Montgomery et al. [13] reported similar effect where NH_3 inhibits the formation of benzene (C_6H_6) in NH_3-CH_4 diffusion flame, of which the soot emission was reported to reduce by a factor of 10 with 20% of NH_3 addition in CH_4. Interestingly, the suppression effect on the formation of C_6H_6 was found to be stronger for NH_3 than N_2, as observed by the reduced concentration of C_2H_2 species in the NH_3-CH_4 flame compared to N_2-CH_4 flame [13]. The N-radicals from NH_3 decomposition would react with C-radicals from conventional hydrocarbons to form cyanide and hydrocarbon amines; thus, the carbon species needed for the formation of benzene is reduced [14]. Cheng et al. [15] investigated the soot formation characteristics of n-heptane co-flow laminar diffusion flames with different blend ratios with ammonia. Results showed that the soot volume fraction (SVF) decreased with the addition of NH_3, implying that the ammonia is effective in inhibiting the formation of PAHs. Even under the turbulent jet diffusion jet flame condition [16], the ammonia addition to ethylene flame was found to reduce soot volume fraction with smaller soot nanoparticles compared to those emitted by neat hydrocarbon fuels, indicating the soot growth process is inhibited. The competition by the nitrogen-based compounds such as HCN, H_3C_2N, and H_3C_3N for the carbon radicals available in flame ultimately reduces the carbon required for soot formation [17]. The impact of NH_3 on soot suppression was found to be more apparent when PAH is larger than 2–3 rings, as was observed in the speciation study in a counterflow flame of NH_3-C_2H_4 [17]. Li et al. [18] reported that NH_3 addition leads to stronger soot suppression effect than H_2, even though both fuels are carbonless. The addition of H_2 in C_2H_4 resulted in the increase of flame temperature; hence, the thermal effect on soot enhancement is more dominant. The soot particles produced from NH_3-doped C_2H_4 flame are more thoroughly oxidized, as evident by the shorter and more tortuous soot morphology. These results indicate the complexity of soot formation process involves not only the chemistry effect, but also the convolution of other factors,

such as thermal and dilution effects, which require extensive experimental data to elucidate the soot formation mechanism.

In the present study, the soot formation characteristics of ammonia blended with ethylene fuel is compared under diffusion jet flame condition. To quantify the soot volume fraction of the blended fuels, the laser extinction method, which is known to provide measurement with high fidelity, is adopted for the present study. The planar flame structure of the NH_3-C_2H_4 flames is investigated via the Abel-transformed OH* chemiluminescence imaging to investigate the main heat release area. The thermal and dilution effects of NH_3 were investigated via the calculation of theoretical NH_3 flame temperature and measured SVF of nitrogen-doped C_2H_4 flames. The present work highlights the characteristics of NH_3-doped fuels in generating soot, paving the way for understanding the formation of soot in actual combustion systems.

2. Experimental

2.1. Burner Setup and Fuels

A co-flow laminar diffusion jet flame burner was utilized to establish the flames for soot measurements. The burner consists of a central jet tube with an inner diameter of 10.5 mm and an outer co-flow tube with inner diameter of 95.6 mm. A flow straightener was used to ensure the supply of co-flow air is uniform to shroud the flame from disturbance. The burner was placed on a motorized traverse, which allows for the spatial translation of axial and radial directions with the accuracy of 0.1 mm, to enable the spatial measurement of soot volume fraction in flame via the laser extinction method. The gaseous fuels used in the present experiment to establish a laminar diffusion flame were ethylene (C_2H_4) and ammonia (NH_3). The blending of the ethylene fuel with ammonia was performed at upstream of the burner prior to ignition at the central jet outlet in diffusion mode. Figure 1 shows the schematic of the burner and flow delivery system. The supply of the co-flow air and gaseous fuels were regulated via mass flow controllers (Sevenstar CS230, accuracy ±1.0 full scale). The co-flow air was maintained constant at 9.91 cm/s for all cases. Blending of the NH_3 with C_2H_4 was performed at different ratios ranging from 9.1 to 50% by volume. Table 1 shows the geometry and operating condition of the burner system. The diluent gas used to blend with ethylene flames was nitrogen (N_2) to decouple the dilution effect from the chemistry effect.

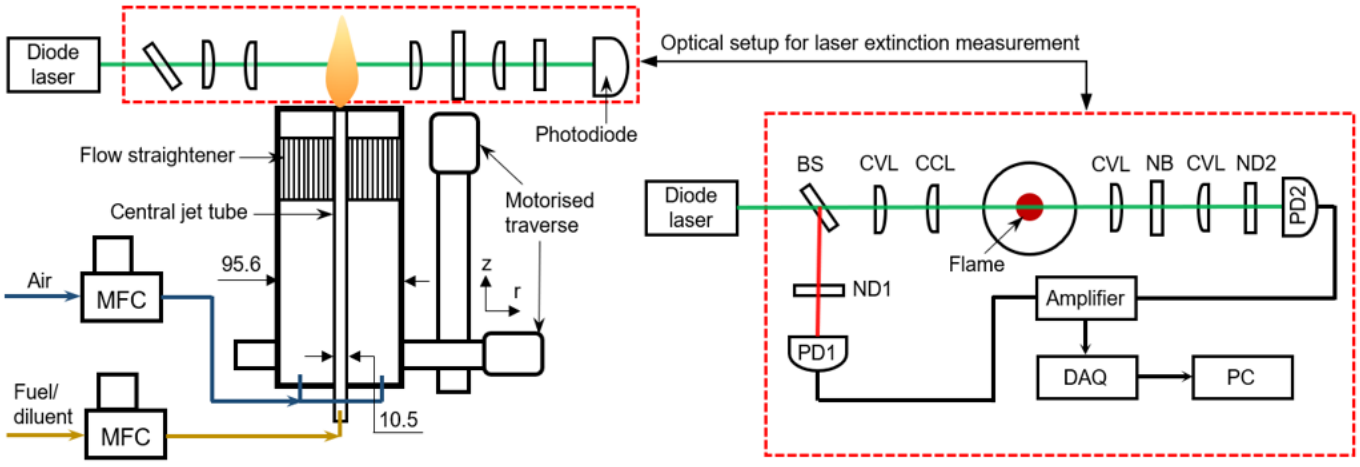

Figure 1. Schematic of the co-flow diffusion jet flame setup and the optical setup for laser extinction measurement. BS: beam splitter, ND: neutral density filter, PD: photodiode, CVL: convex lens, CCL: concave lens, NB: narrow band filter, AMP: amplifier, DAQ: data acquisition board. Dimensions are in millimeters.

Table 1. Geometry and operating conditions of the burner system.

Jet diameter (mm)	10.5
Co-flow tube diameter (mm)	95.6
Co-flow medium	Air
Co-flow velocity (cm/s)	9.91
NH_3 blend fraction (vol.%)	9.1–50.0
NH_3 flow rate (L/min)	0.02–0.2
C_2H_4 flow rate (L/min)	0.2

2.2. Measurement Techniques

2.2.1. OH* Chemiluminescence Imaging

Imaging of the via OH* chemiluminescence signal emitted from the laminar diffusion jet flame was performed using a CCD camera (LaVision SX-4M) coupled with an intensifier (IRO X) fitted with a UV lens (Nikon 85 mm) and a bandpass filter centered at 306.4 nm ±1 nm (Thorlabs). The intensifier was set to 100% gain, 900,000 ns gate, 150 ns delay, and 30 Hz imaging frequency. For each case, 150 frames with the spatial resolution of 0.2005 mm/pixel were taken for averaging after the established flame was stabilized. The actual flame images were captured using a digital single-lens reflex camera (Sony A35) with the setting of ISO 100, f1.8, and 1/100 s. For image post-processing, Abel transformation was performed to obtain the 2D planar OH* signals representative of the flame structure at center plane.

2.2.2. Laser Extinction Measurement Technique

The schematic of the laser cavity measurement system is shown in Figure 1. A monochromic diode laser (Laserwave, LWRL638–150 mW, 638 nm wavelength, 150 mW maximum power) was used as the detection laser source. A relative long near IR region ensures a good validity of Rayleigh Approximation for the detection of soot volume fraction. Moreover, the polycyclic aromatic hydrocarbons (PAHs) absorption of laser energy can be ignored in the region [19]. Thus, the λ_e = 638 nm was selected as an optimal detection wavelength for the present study.

The laser beam is split into a reference beam (about 1% of the total laser energy) and a main measuring beam (about 99% of total energy) by a beam splitter (Thorlabs BSF10-A). The reference beam intensity is measured by a photodiode (Thorlabs SM05PD1A Silicon Photodiode, 350–1100 nm) equipped with a neutral density filter (ND1: Thorlabs NE20A-A, optical density = 2.0), and the laser energy is proportionally converted into a small electric current i_{ref}. The main probe beam passes through a concave lens (Thorlabs LC4888, −100 mm focal length) and a convex lens (Thorlabs LA1461-A, 250 mm focal length) to be collimated into a thin Gaussian beam before entering the target flame. Therefore, the finest possible spatial resolution of the measurements is approximately 200 μm [3]. Another ND filter (Thorlabs NE10A-A, optical density = 1.0) and a NB filter (FL635-10 -Ø1″ Laser Line Filter, CWL = 635 ± 2 nm, FWHM = 10 ± 2 nm) are used to attenuate the probe laser intensity and filter the flame luminosity, respectively. The main laser beam is measured using an identical photodiode for the reference beam and produces a photocurrent i_p, which is proportional to the attenuated laser beam. The currents from the two photodiodes i_{ref} and i_p are collected and compared by a logarithmic amplifier (Texas Instrument LOG104), and the output voltage of the amplifier V_{out} is given as:

$$V_{out} = C \log_{10} \frac{i_p}{i_{ref}} \quad (1)$$

where the amplification constant $C = 0.5$ V is provided by the manufacturer. The voltage is recorded by using a data acquisition board (NI USB-6009) at a 12-bit resolution and at 150 Hz for 10 s. By taking the ratio between the reference beam and main probe beam's photocurrents via the logarithm amplifier, measurement uncertainty caused by the energy

output fluctuation of the diode laser source could be cancelled, as the ratio of the two beams remains a constant given when the optics are stable. The values of V_{out} when the flame is on (with soot) and off (without soot) are measured separately. Providing the photocurrent is proportional to the laser intensity, the ratio of I_t and I_i in Equation (3) is evaluated, and hence, P_0 is obtained.

2.3. Laser Extinction Theory

The laser extinction technique [20–22] is used to quantitatively measure the soot volume fraction distribution f_V in the target flames. The extinction measurement is based on the principle that when a laser beam passes through a flame containing soot particles, the intensity of the beam will reduce due to the absorption and scattering of soot. The laser beam's power reduction follows Lambert–Beer Law [23,24] as shown in Equation (2):

$$\frac{\Delta I}{I} = -K_e \Delta x \tag{2}$$

where I is the incident laser beam intensity, ΔI is the reduction of the incident laser beam intensity after travelling through a small distance Δx in the probe volume, and K_e is the extinction coefficient determined by the local volume fraction and the optical properties of soot. By integrating Equation (3) along x, we obtain:

$$-\ln \frac{I_t}{I_i} = \int_{I_i}^{I_t} \frac{\mathrm{d}I}{I} = \int_{-\infty}^{+\infty} K_e \mathrm{d}x = P_0 \tag{3}$$

where I_t and I_i are the intensities of the laser beam before and after the it passes through the flame, respectively. The projection value P_0 represents logarithmic extinction of the laser intensity. The extinction of a laser beam is caused by the absorption and scattering of soot particle in flame [25,26]. The relative contribution of scattering and absorption to total extinction is determined by the ratio of incident beam wavelength λ_e and the particle diameter D [27]. When λ_e is much larger than D, the interaction between the beam and particles are in the Rayleigh Approximation Region [28]. Within the Rayleigh Region, the total extinction coefficient can be considered as the arithmetic sum of scattering coefficient K_s and absorption coefficient K_a. The value of K_s could be estimated by multiplying the total scattering cross section area of soot and the relative frequency of occurrence of scattering [27], as shown in Equation (4):

$$K_s = N \frac{8\pi}{3} \left(\frac{\pi}{\lambda_e} \right)^4 \frac{F(m)}{4} \int_0^{\infty} P(D) D^6 \mathrm{d}D \tag{4}$$

where m is the complex refractive index of soot, $P(D)$ is the probability distribution function of soot particles' diameter, and $F(m)$ is the scattering function of soot particles, which could be calculated as a function of m:

$$F(m) = \left| \frac{m^2 - 1}{m^2 + 2} \right|^2 \tag{5}$$

Similarly, the absorption coefficient of soot particles K_a can be calculated as the product of extinction cross section and the particle number density:

$$K_a = N \frac{\pi^2}{\lambda_e} E(m) \int_0^{\infty} P(D) D^3 \mathrm{d}D \tag{6}$$

where the absorption function $E(m)$ is given by the imaginary part of a function of m as shown in Equation (7):

$$E(m) = -\mathrm{Im}\left(\frac{m^2 - 1}{m^2 + 2} \right) \tag{7}$$

By combining Equations from (1) to (6), the ratio of K_s and K_a is proportional to D/λ_e. A non-dimensional size parameter $\mathrm{d} = \pi D/\lambda_e$ is introduced as a criterion for the validity of Rayleigh Approximation. When $\mathrm{d} < 0.3$, the scattering is negligible, and one can consider $K_e = K_a$ [29]. In the present study, the soot particles produced in the base undiluted flame are mostly small than 60 nm in diameter [30], which falls in the Rayleigh Region considering the detection laser used is λ_e = 638 nm. Moreover, the NH_3 diluted cases produce smaller particles than the reference undiluted case, which ensures an even better validity of the Rayleigh Approximation. Therefore, the f_V and K_e can be linearly related as:

$$K_e = K_a = \frac{6\pi E(m)}{\lambda_e} f_V \tag{8}$$

The projection value of P_0 along each chord position y across a certain height of the flame is measured experimentally. By applying inverse Abel transform [22] to Equation (3), the extinction coefficient as a function along radial distance in a flame height $K_e(r)$ could be obtained from the measured projection value along each chord position $P_0(y)$, as:

$$K_e(r) = -\frac{1}{\pi}\int_y^\infty \frac{P_0'(y)}{\sqrt{y^2 - r^2}}\mathrm{d}y \tag{9}$$

where $P_0'(y)$ is the first-order differential of $P_0(y)$. Equation (9) is solved numerically by using the one-dimensional discrete three-point Abel transform scheme [31], and hence, the soot volume fraction as a function of radial distance $f_V(r)$ can be evaluated.

2.4. Validation of the Laser Extinction Technique

Validation of the present laser extinction measurement method is performed by comparing with the soot data obtained from a jet diffusion flame via the 2D planar laser-induced incandescence (LII) measurement method [20]. The LII method is based on the principle of heating the soot particle with a high-power laser to temperature high enough to emit measurable quasi-blackbody radiation. Subsequently, the emission of the radiation is recorded with gate detection technique to resolve spatially to derive the particle-distribution or volume-fraction measurements related to the primary-particle size information [19]. In the present study, the target flame used for validation is a standard diffusion co-flow flame was established with 0.18 LPM of ethylene diffusion flame, surrounded by the co-flow of air supplied at 35.0 LPM [20]. The flame appearance is a typical cone-shape jet flame at laminar condition. Figure 2 shows the half-plane measurement of the SVF for a standard ethylene diffusion at different height above burner (HAB) derived from the two methods. The y-abscissa represents the burner centerline, while the x-abscissa represents the radial displacement from the burner centerline. Near the jet exit nozzle at z = 15 mm, the SVF is seen to peak at a distance from the centerline. Further increase in flame height location shows the peak SVF shifts towards the jet flame centerline. At about z = 50 mm, the peak of SVF is located at the jet centerline with slightly lower magnitude compared to the peaks at flame wings (z = 30–35 mm).

The laser extinction method is able to reproduce the SVF trends rather closely at all axial heights above the burner including the peaking location and magnitude, in spite of some slight discrepancy observed at the center region of the flame and at height above burner of z > 40 mm. The discrepancy could be due to the fluctuation of the flame; in particular, the flame is more susceptible to the dynamic of flame interaction with the co-flow at higher HAB. Further, the uncertainty induced by the Abel transformation of LII and extinction method due to signal trapping could be another reason for the discrepancy. Nevertheless, the validation shows that laser extinction method is able to provide quantitative measurement with high confidence for SVF up to HAB = 40 mm. It should be noted that the LII data were calibrated against the extinction method by using the procedure described in [21,22]. In other words, the LII results are not independent of the extinction. As the calibration process involves matching the total integrated SVF over the flame radial

distance between the extinction and LII [21,22], the good agreements between the two techniques in both maximum SVF and profile of SVF along radial distance demonstrated that the extinction measurement is sufficiently accurate to resolve the gradient of SVF along with radial distance without losing information.

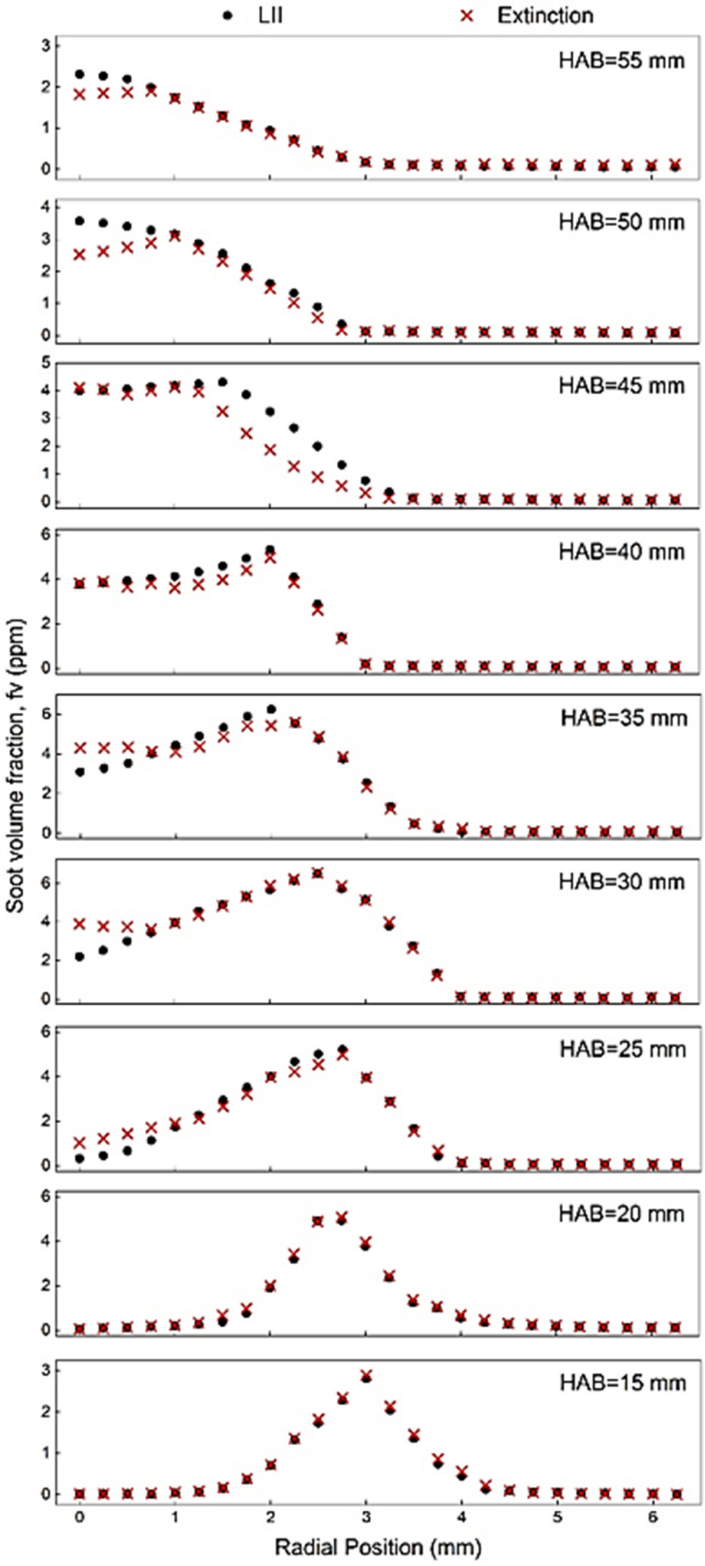

Figure 2. Comparison of the soot volume fraction of a standard ethylene diffusion jet flame at different heights above the burner measured by laser extinction and LII methods.

A detailed uncertainty analysis for the extinction measurement system was performed in our previous publication [22]. Although combined uncertainty was calculated for the multi-pass system in the study [22], the conclusion is applicable for the single-pass system that was used in the present study, as the cavity configuration does not change the uncertainties contributed by the flame fluctuation, the absorption function E(m), and Abel transform. Via a detailed error propagation analysis [22] and a field reconstruction simulation [22,31], it was found that the uncertainty arising due to tomographic inversion and discretization of the Abel transform is estimated to be around 10–20% at the peak soot volume fraction (SVF) position in flame. The uncertainty caused by E(m) is difficult to quantitatively estimate. Some previous studies shows that the value of m and E(m) are both wavelength and fuel dependent [32,33]. The discrepancy on the reported E(m) for the soot produced in the hydrocarbon flames that are similar to the present study can be as large as 40% [34,35]. Using the value of 0.26 in the present study [35] is likely to underestimate the SVF deduced by extinction measurement. However, given that the Rayleigh Approximation may still overestimate SVF (by neglecting scattering) [35], further accurate values of E(m) would still directly improve the accuracy of the extinction method. Therefore, considering the large uncertainty associated with E(m), the experimentally obtained values of K_e alongside with the SVF values are reported in the Supplementary Materials. The values of K_e are independent of any assumptions about E(m) and can be useful in the validation of future models.

3. Results and Discussion

3.1. Flame Imaging and OH Chemiluminescence*

The establishment of laminar co-flow diffusion jet flames enables a stable cone flame anchored at the burner outlet for soot measurement. Figure 3 shows the flame appearances of the diffusion jet flames of ethylene doped with different concentrations of NH_3. It is observed that the flame heights do not differ much for the range of blends tested, with all the flame heights hovering around 90 mm from the nozzle exit, but the inner cone of the flame is noticeably increased in height with the increasing NH_3 blend ratio. It is important to note that the blending of NH_3 to the initial 0.20 LPM of ethylene results in the increase of total flow rate, and hence, the flow velocity at the exit of the burner varies. Nonetheless, the carbon content for all the flames is the same; hence, the soot formation tendency is compared under the same amount of carbon compounds. The fuel is then fed to the reacting flame front where the reaction takes place in the luminous zone. The increasing area exhibited by the inner cone shows that a higher NH_3 blend fraction results in a delayed reaction at the flame front. This is expected as the NH_3 is known to have low flame speed, high activation energy, and longer ignition delay time [36].

The Abel-transformed OH* chemiluminescence imaging shows that the heat release region differs rather significantly for different C_2H_4-NH_3 blend ratios. At the low NH_3 blend, the heat release region is noticeably larger with higher OH* intensity near the flame root and the center region downstream of the inner cone. With the increase of NH_3 blend fraction, the peak OH* signal is seen to shift further downstream towards the flame tip region, in accordance with the elongated inner cone. This concurs with other experimental study, which shows the addition of NH_3 decreases the flame temperature at the early stage of the flame and increase the flame temperature at the post stage [12]; thus, the soot loading is shifted correspondingly from the flame wing to the flame centerline. By blending 44.4% vol. of NH_3, the OH* chemiluminescence emission intensity is seen to weaken relative to the low NH_3 blends, owing to the chemistry effect of the blend mixture and inherent low heating value of NH_3. The OH* intensity signal at the flame root is also seen to reduce at a higher fraction of NH_3, implying that the NH_3-enriched flame is more prone to flame blowout, should the flame stabilization mechanism be affected by insufficient reactivity and heat loss to the burner rim.

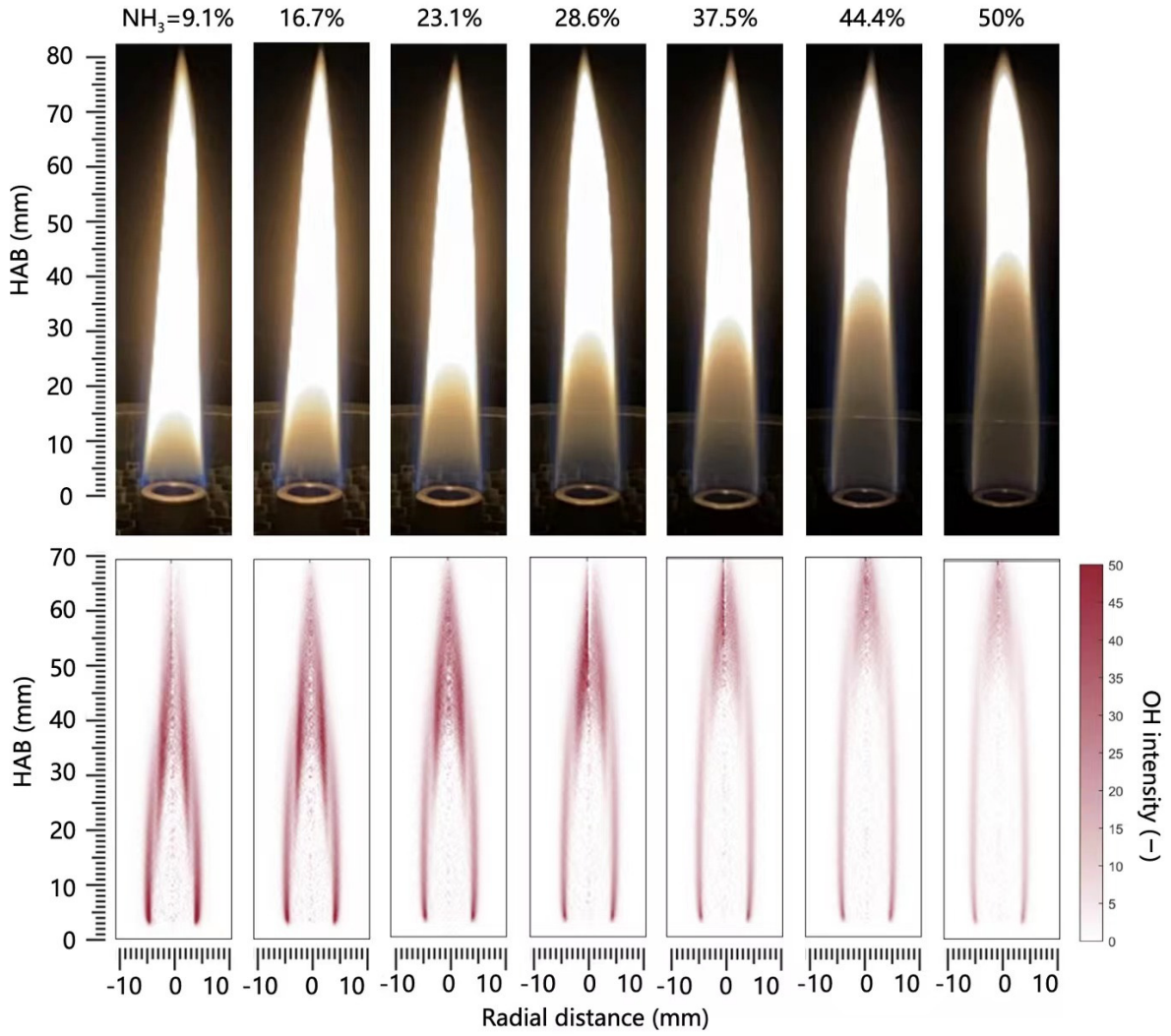

Figure 3. Flame images and the corresponding OH* chemiluminescence images of ethylene diffusion jet flame doped with ammonia at different volume percentages.

To account for the effect of dilution, the measurement of the SVF for ethylene flame doped with different N_2 blend fractions is performed. Similar to the C_2H_4-NH_3 set of flames, the C_2H_4 flow rate is fixed while the N_2 is blended prior to burning in diffusion mode. In general, the flames established were stable with similar flame heights of around 100 mm for the range tested, as shown in Figure 4. Although the flame length (luminous yellowish flame region) does not vary significantly between the flames, the inner cone region shows an increasing height with higher fraction of N_2. Compared with the C_2H_4-NH_3 flames of the same total flow rate, the growth in size for the inner cone is less, implying the reactivity of the N_2-doped ethylene flame is higher than the NH_3-doped counterparts. This is validated by the corresponding Abel-transformed OH* flame images, where the flame structure is similar for all the flame tested. The flame wings and flame centerline region downstream of the inner cone show high intensity of the OH* signal, indicating the dilution of N_2 has insignificant impact on the fuel chemistry reaction. Figure 5 shows the comparison of the flame heights for the NH_3- and N_2-doped C_2H_4 diffusion jet flames. The luminous flame height is defined as the length of the flame from the burner outlet to the tip of the flame, whereas the length of the inner cone is defined as the nozzle outlet to the tip of the cone located at the centerline. The NH_3-doped C_2H_4 flames show a consistently shorter flame length than N_2-doped flames, but the inner cone length for the former is longer than the latter, in particular for C_2H_4 flames with an NH_3 addition at $\geq$30% by vol.

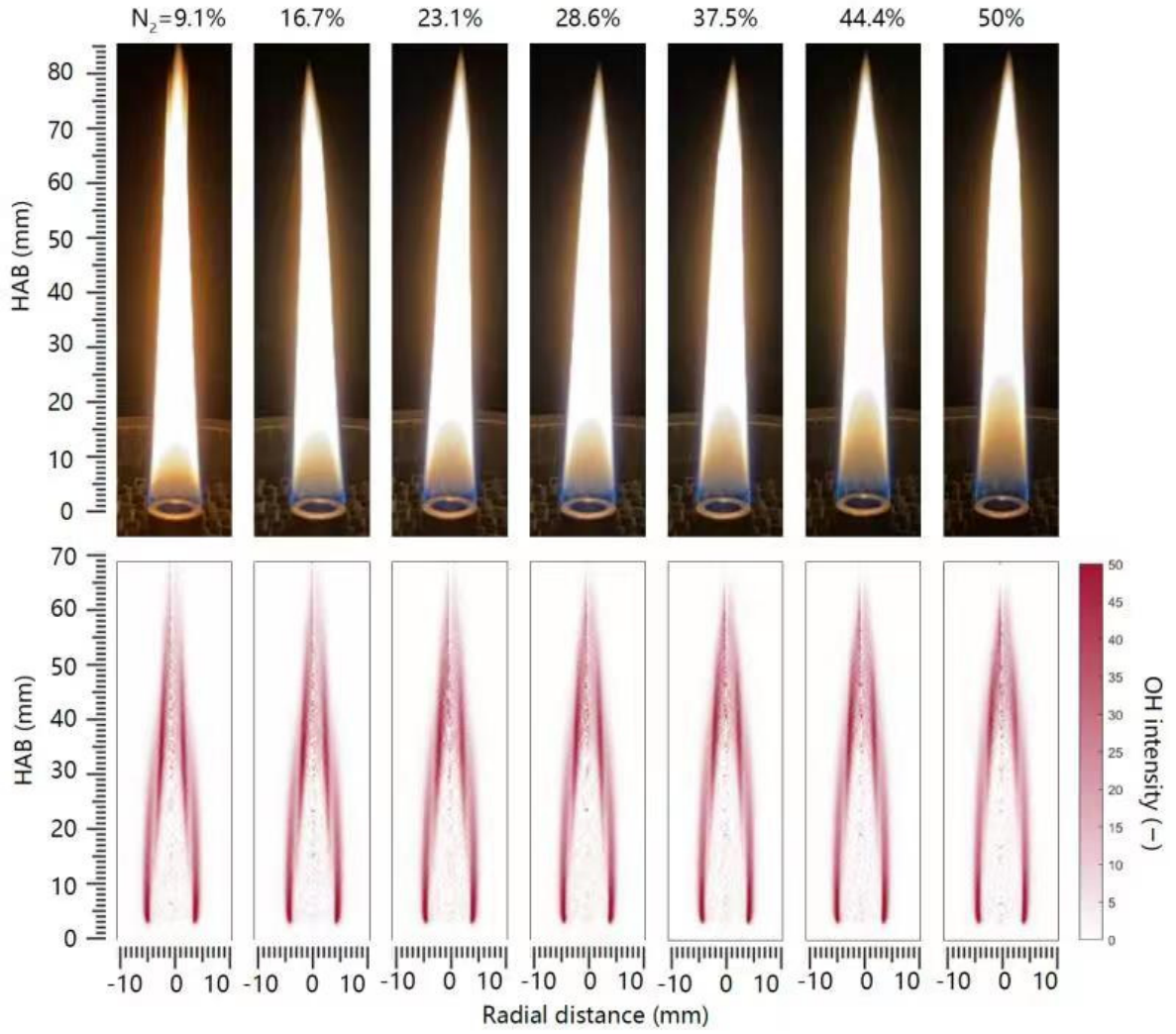

Figure 4. Flame images and the corresponding OH* chemiluminescence images of ethylene diffusion jet flame added with nitrogen at different volume percentages.

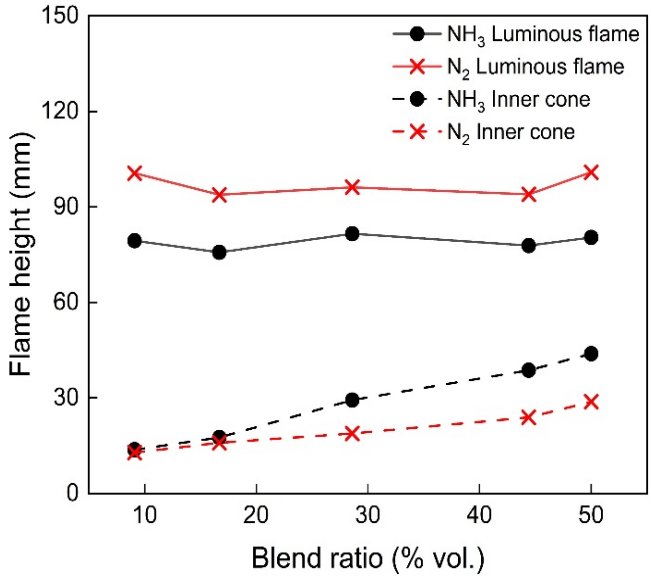

Figure 5. Comparison of the flame height of C_2H_4 luminous flame height and inner cone as a function of different NH_3 and N_2 blend fractions.

3.2. Soot Volume Fractions

3.2.1. Effect of Ammonia

Measurements of the soot volume fraction for ammonia-blended ethylene flames were performed at different HAB to characterize the planar soot distribution. Due to the axisymmetric nature of the jet diffusion flame, measurements were conducted at the half-plane of the flame. Figure 6 shows the radial soot volume fraction of C_2H_4-NH_3 flames measured at HAB = 25, 35, and 45 mm from the burner centerline. The measurements were conducted at the spatial distance of 0.25 mm for ethylene flame with NH_3 blend fraction of 18.2%, 25.0%, and 30.8% by volume. Comparison of the radial SVF profiles shows a distinct difference in the peaking location of SVF. For the lower NH_3 fraction, the SVF peaks at radial location between 2 and 3 mm from centerline with a higher peak SVF value compared to flames with higher NH_3 fractions. This also implies the flame has wider flame wing with higher reactivity that is prone to form more soot. An increase of NH_3 to 25% results in a drastic decrease of SVF at all HAB. The peak location of SVF shifts towards the centerline, indicating the thinning of the flame reaction zone with reduced reactivity. The reduction of soot can be attributed to the reduction of benzene (C_6H_6) and polycyclic aromatic hydrocarbons (PAH), which are the precursors needed for the growth and formation of soot [12,14].

Interestingly, a further increase of NH_3 to 30.8% results in marginal decrease of SVF, but the flame structure remains the same as those of 25.0% NH_3, as evident by the same peak SVF locations. At z = 45 mm, the peak of SVF is not reflected in the cases with >25% NH_3 blend fraction, but plateaus with an almost constant value of SVF of 1 ppm. The SVF at HAB = 45 mm is reduced by a factor of 2 for the flame with 25% NH_3 as compared to the peak SVF of 18.2% NH_3 in ethylene flame. The varying degree of soot reduction can be explained by the rate-limiting step of benzene formation. It is known that the formation of C_6H_6 from C_2H_4 decomposition follows the pathway of $C_2H_4 \rightarrow C_2H_3 \rightarrow C_2H_2 \rightarrow C_3H_4$–P $\rightarrow C_3H_3 \rightarrow C_6H_6$. The C_6H_6 then proceeds to form PAH via the hydrogen-abstraction C2H2-addition (HACA) growth mechanism [37]. The plausible C_6H_6 inhibitory route in the NH3-doped C_2H_4 flame occurs via the suppression of C_2H_3 species. The dominant C_3H_3 formation pathways are $C_2H_4 + \mathrm{H} \leftrightarrow C_2H_3 + H_2$ $(R1)$, $C_2H_3(+M) \leftrightarrow C_2H_2 + H(+M)$ $(R2)$, and $C_2H_2 + CH_2 \leftrightarrow C_3H_3 + H$ $(R3)$ based on the kinetics elucidated via the AramcoMech mechanism [14]. The H_2 produced from the pyrolysis of NH_3 suppresses reaction R1, and thus, the formation of C_2H_3. A consequence of this is the formation of C_2H_2 and C_3H_3 is inhibited.

Since the formation of C_6H_6 is mainly governed by the reactions $2C_3H_3 => C_6H_6$ $(R4)$ and $C_6H_6 + H(+M) = C_6H_6(+M)$ $(R5)$ at 1400 K, the lack of C_2H_3 and C_3H_3 radicals directly inhibits the formation of C_6H_6. The importance of C_3H_3 for the inception of C_6H_6 is also corroborated in another non-premixed NH_3-C_2H_4 reaction mechanism study via the reactions of $C_2H_2 + CH_2 = C_3H_3 + H$ $(R6)$ and $C_3H_3 + OH \leftrightarrow C_2H_3 + HCO$ $(R7)$ [12]. Further, the formation of propyne (C_3H_4-P) is disrupted as a result of a higher H_2 mole fraction produced from NH_3 decomposition, i.e., via the reaction $C_3H_4 - \mathrm{P} + \mathrm{H} \leftrightarrow C_3H_3 + H_2$ $(R8)$, which inhibits the conversion of C_3H_4-P into C_3H_3 [14]. In short, the intermediate species of C_2H_2, C_3H_3, and C_3H_4-P, which are essential for the formation of C_6H_6, are affected when NH_3 is added to C_2H_4 flame. Instead, the interaction between nitrogen and hydrocarbon leads to new reaction pathway to produce hydrocarbon amines such as HCN, CH_2NH, CH_2CHNH_2, and CH_3NH_2, amongst others, which reduces the carbon-based species required in the soot aggregation process [12,38]. At higher NH_3 blend fraction, there is significantly lesser amount of carbon atoms available for C_6H_6 formation, which explains the reduction of soot is not as evident compared to low NH_3 blend fraction as shown in Figure 6. Other than benzene, other soot precursors such as naphthalene, phenanthrene, and pyrene were also shown to decrease with increasing ammonia fraction [12]; hence, the growth of nascent soot is disrupted.

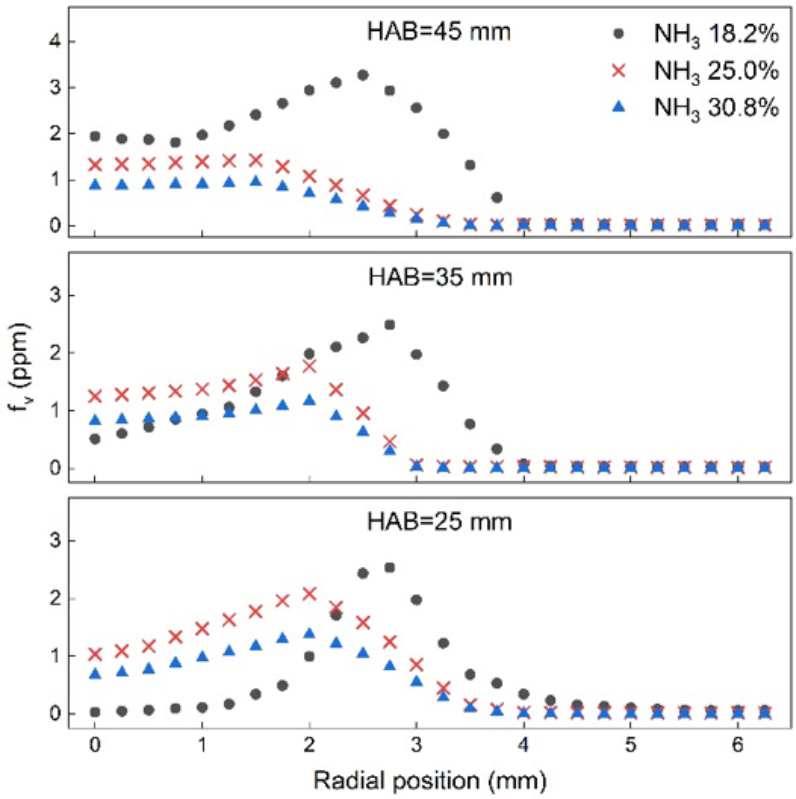

Figure 6. Half-plane radial distribution of SVF for ethylene flames blended with NH_3 of different volume at HAB = 25, 35, and 45 mm. The C_2H_4 was supplied at constant flow rate of 0.18 LPM.

The normalized SVF of C_2H_4-NH_3 flames and neat C_2H_4 diffusion flame at the axial centerline are shown in Figure 7a. Being a sooty flame, the C_2H_4 flame produces the largest amount of soot, followed by the increasing blend fraction of NH_3. A non-monotonic decrease of soot production is reflected, where the 9.1% NH_3 blend shows a decrease by more than 50% compared to the neat C_2H_4 flame, whereas the 16.7% NH_3 blend shows a drastic reduction of SVF by approximately 80%. This shows that a relatively low blend ratio of NH_3 with hydrocarbon flame can achieve a significant improvement in soot emissions. From the NH_3 decomposition perspective, N-containing species react with C-based species to form cyanogen, cyanides, and hydrocarbon amines, thus reducing the amount of carbon for hydrocarbon growth chain [14,17]. For instance, hydrogen cyanide (HCN) is produced via the reaction $H_2CN \leftrightarrow HCN + H$ $(R9)$, in which the H_2CN is produced from the reaction $NH_3 + CH \leftrightarrow H_2CN + 2H$ $(R10)$ [14]. A similar conclusion was reported by the study [39], where the introduction of ammonia results in the increase of HCN and CN, highlighting the competition between NH_3 and O over carbon atoms, thereby causing the decrease of CO and CO_2 concentrations [40].

Concurrently, the NO formed from NH_3 oxidation would enhance the consumption of C_2H via $C_2H + NO \leftrightarrow HCN + CO$ $(R11)$ and $C_2H + NO \leftrightarrow CN + HCO$ $(R12)$, which then suppresses the formation of C_3H_4-P, leading to the decrease of C_6H_6 formation. However, the gradient of soot reduction decreases with further addition of NH_3, in which the increase of NH_3 to 23.1% by volume does not result in large drop in soot production, as opposed to the lower HN_3 blend fractions. Another interesting observation is that the peak SVF at the centerline axial profile is shifted further downstream with increasing NH_3 blend fraction. This concurs with the global phenomena of increasing inner flame cone length as observed in Figure 3, thereby pushing the main heat release rate further downstream towards the flame tip region. The effect of NH_3 addition was reflected not only in the overall decrease of soot formation, but also the soot particle size was shown

to reduce [12,38]. Figure 7b shows the non-linear decrease of SVF with the addition of increasing ammonia fraction in C2H4 flames.

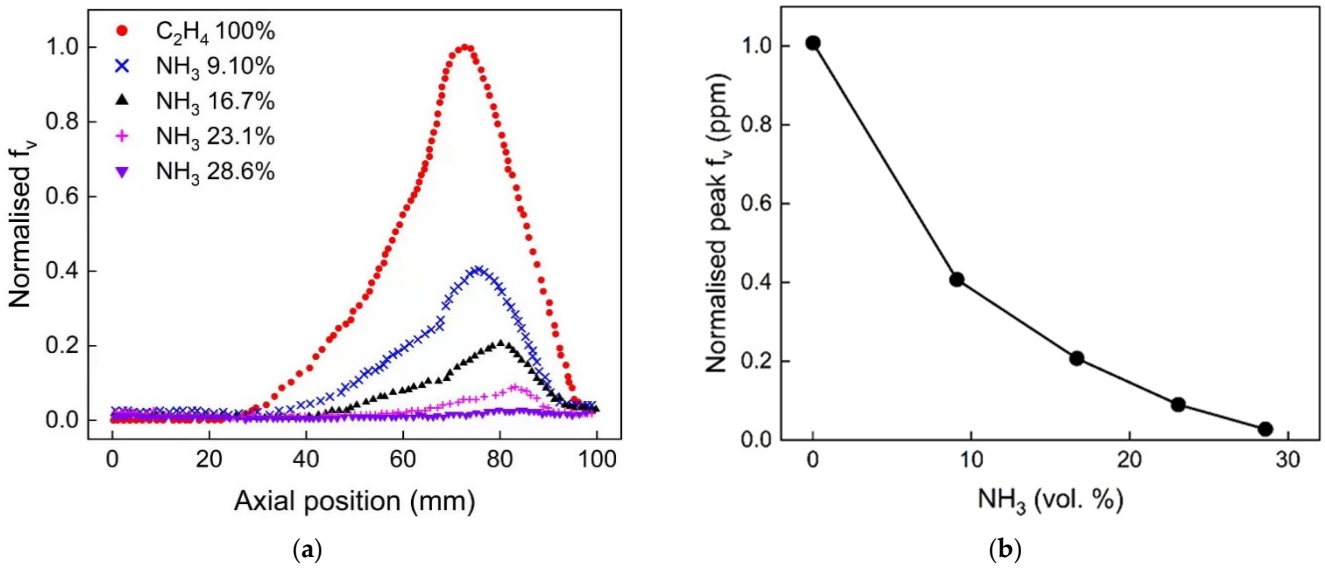

(**a**) (**b**)

Figure 7. Comparison of the (**a**) centerline axial profile of normalized SVF and (**b**) peak SVF for different C_2H_4-NH_3 flames with the baseline C_2H_4 flame. The C_2H_4 was supplied at constant flow rate of 0.18 LPM.

3.2.2. Factorizing of the Soot Suppression Effects

A sensible way to investigate the factors that inhibit the soot formation in an ammonia-diluted flame was proposed by Law and coworkers [41,42] and has been extensively used by other following researchers [21,43,44]. Law and coworkers [41] suggested that the non-sooting additives prohibit the soot formation in flames via three ways: (1) dilute the reactants (dilution effect), (2) lower the reaction temperature for soot formation (thermal effect), and (3) participate and slow down the chemical reactions for soot formation (chemical effect).

To investigate the chemistry effect of NH_3 on soot formation, the dilution effect is decoupled by comparing with the N_2-blended C_2H_4 flame. Figure 8 shows the radial distribution of SVF between 10% N_2- and 10% NH_3-doped ethylene diffusion flames. The net difference between the two profiles signifies the chemical influence of NH_3 on soot suppression. The addition of N_2 lowers the flame adiabatic flame temperature, thereby resulting in a decrease of the hydrocarbon growth rate and soot formation process [45]. In addition, the presence of N_2 reduces the collision frequency between the fuels and its products, which contributes to the suppression of soot formation [13]. The peak SVF locations are similar at different HAB for both profiles but shift towards the centerline axis as the HAB increases. This is expected as the flame shape changes with respect to flame height. Since the addition of N_2 lowers the C_6H_6 concentration through dilution and thermal influences, the net difference between the NH_3 and N_2 profiles suggests the chemical influence on C_6H_6 formation rates. A speciation experimental study has reported that the difference of C_2H_2 level is similar between N_2- and NH_3-doped methane flames, implying that NH_3 most likely affect the formation of C_6H_6 by disrupting the formation of other precursors such as C_3H_6, C_4H_6, or C_3H_4-P [13].

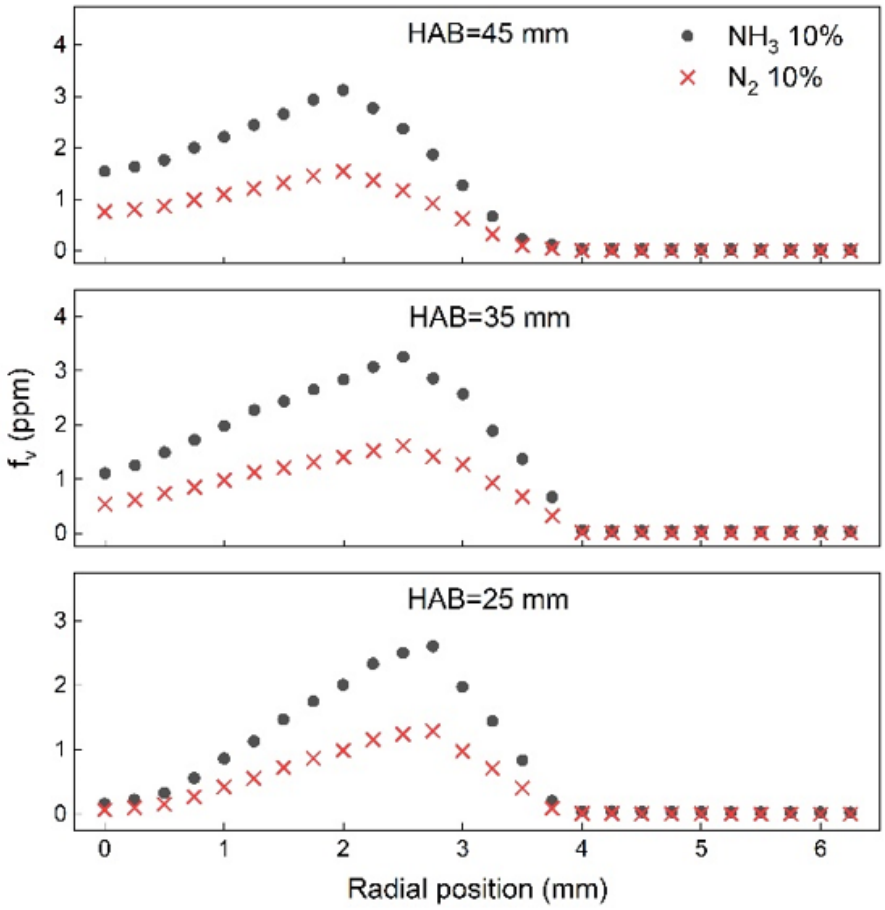

Figure 8. Radial distribution of the SVF for 10% of NH_3 and N_2 by vol. added to ethylene diffusion flame. The C_2H_4 was supplied at constant flow rate of 0.18 LPM.

The results shown in Figure 8 indicate that temperature is key information to understand the soot formation footprint in the flame. However, it is not possible to perform a thorough soot formation analysis in a 2D SVF map against the temperature distribution in the corresponding flames. By using a simplified one-step soot reaction model involving the Arrhenius term, the relative importance of the three factors in reducing soot formation could be obtained and compared. Gülder et al. [43,44] proposed and verified that the maximum soot mass fraction (SVF_{max}) in the centerline of a diffusion jet flame could be linearly related to a term as below:

$$\mathrm{SVF}_{\max} = B_P H^{\frac{1}{2}} X_{F,0} e^{\frac{-E_a}{R_0 T_f}} \tag{10}$$

where B_p is a constant for all cases, and H is the visible flame height, whose square root is considered as proportional to the residence time for soot formation along flame center [21,43]. $X_{F,0}$ is the ethylene molar fraction in the in the coming fuel jet. The value of the global activation energy for soot formation in ethylene flames 200 kJ/mol is taken from the [46]. R_0 is the ideal gas constant, and the flame temperature T_f is estimated using the ultra-fast reaction model for the non-premixed flame [21], as:

$$T_f = \xi_{st} Y_{F,0} \frac{Q}{c_p} + \xi_{st}(T_{F,0} - T_{O,0}) + T_{O,0} \tag{11}$$

where $Y_{F,0}$ and $Y_{O,0}$ are the boundary mass fractions of fuel and oxygen at the fuel side and oxidizer side, respectively. In the present study, $Y_{F,0}$ = 1, as ethylene and ammonia are all fuels for the flame, and $Y_{O,0}$ = 0.233 for the air, which is used as oxidizer for all cases.

$T_{F,0}$ and $T_{O,0}$ are the boundary temperatures for fuel and oxidizer, respectively, which is 298 K for the present study. Q is the heat value of the fuel mixture, which is obtained by calculating the mass-fraction-weighted mean low heat value (LHV) of the mixture as:

$$Q = Y_a Q_a + Y_e Q_e \tag{12}$$

where Y_a, Q_a, and Y_e, Q_e are mass fractions and LHVs for ammonia and ethylene, respectively. Here, we take Q_a = 18.8 MJ/kg [5] and Q_e = 47.7 MJ/kg [47]. The mixture fraction for non-premixed flame ξ is defined by:

$$\xi = \frac{\left(Y_F - \frac{Y_O}{s}\right) - \left(Y_F - \frac{Y_O}{s}\right)_{O,0}}{\left(Y_F - \frac{Y_O}{s}\right)_{F,0} - \left(Y_F - \frac{Y_O}{s}\right)_{O,0}} \tag{13}$$

The subscript 0 means the boundary values, and S is the mass ratio of the oxygen and fuel for a complete combustion. The flame temperature T_f is hence calculated against the blending ratio of ammonia in the fuel jet, and the results are plotted in the Figure 9 using solid red line. It shows that the heat value of ammonia is lower than ethylene by 61%; however, because significantly less air is required by ammonia, and hence a higher mixture fraction at the stoichiometric location ξ_{st} can be achieved, the flame temperature for pure ammonia flame is only roughly 5% lower than that of the pure ethylene case, as shown in the figure.

The contribution of dilution effect, thermal effect, and chemical effect of ammonia addition to the soot formation can be analyzed separately. By taking the value of T_f as a constant of pure ethylene case, we can obtain the SVF_{max} (with terms H and B_p) against ammonia's blending ratio. The SVFs are then normalized against the pure ethylene flame. Considering the flame heights H are very similar across all tested cases, and B_p is a constant, they can be cancelled, and the normalized SVF at a constant flame temperature is calculated as showed (blue dashed line) in the Figure 9. As in the calculation, the temperature is set as a constant; therefore, the reduction of SVF_{max} is entirely caused by the dilution effect. Unsurprisingly, the dilution effect of ammonia to the soot formation presents a linear manner as the blue dashed line is a straight line, with a gradient of 1. Next, the calculated T_f from Equation (11) is inserted into Equation (10), and normalize the calculated SVF_{max}, and the results are plotted in the Figure 9 using a solid green line. As the actual T_f values are used for the calculation, the thermal effect on soot reduction could be obtained by comparing the SVF_{max} obtained from the previous step (blue dashed line). Finally, by comparing against the measured SVF_{max} (shown as dots in Figure 9), the chemical effect of ammonia for soot reduction can be evaluated. Obviously, the reduction of soot mainly attributes to the dilution and chemical effects of ammonia. The conclusion is in a good agreement with the results shown in Figure 8. The contribution of thermal effect is small compared to the other two. This is due to (1) an insignificant temperature reduction with the ammonia addition, and (2) a relatively small global activation energy of soot formation for ethylene. A chemical analysis will be performed in detail in our future study.

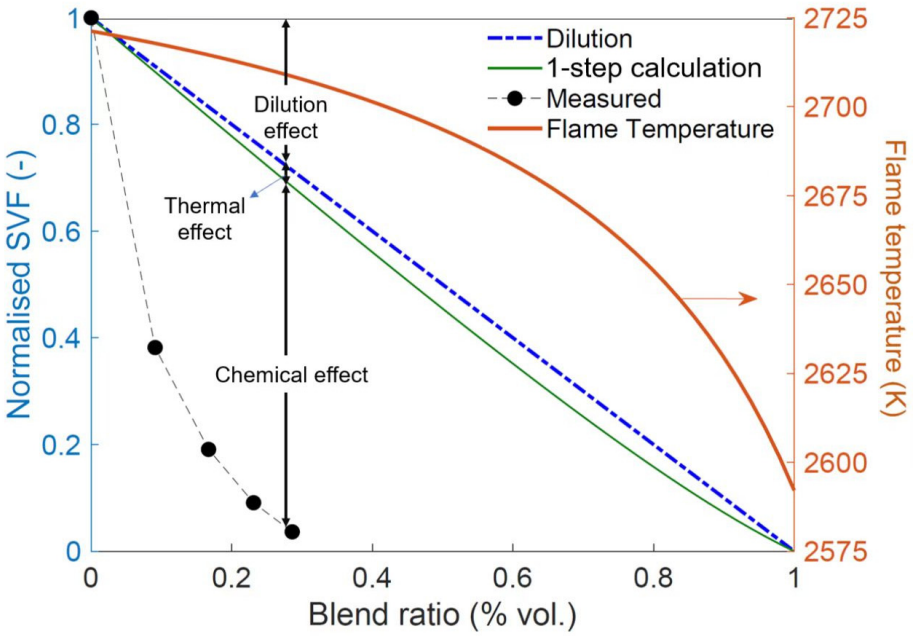

Figure 9. Normalized measured maximum soot volume fraction SVF (dots) at the flame centerline as a function of the volumetric percentage of ammonia (left axis). Calculated flame temperature (right axis). Model predictions: concentration change via dilution (blue dashed line), single-step model (green solid line).

4. Conclusions

The soot formation tendency of NH_3-doped C_2H_4 flames was investigated via the establishment of a co-flow laminar diffusion jet. Flame imaging shows that the flame physical appearances for NH_3-doped C_2H_4 flames have similar flame heights, but the inner cone height increases with the NH_3 blend fraction. Similar flame structure was observed for the N_2-doped C_2H_4 flame at different N_2 fractions. Despite the similar flame heights, OH* chemiluminescence imaging revealed the peak heat release shifts from flame wings to the centerline flame region with increasing NH_3/N_2 blend fractions, while the intensity of the OH* emission decreased, indicating reduced flame reactivity. Measurement of the soot volume fraction within the flame using the laser extinction method showed that the effect of NH_3 on soot reduction is evident. At different HAB, the SVF was observed to reduce with increasing NH_3 blend fraction, largely attributable to the reduction of key intermediate species such as C_2H_2, C_3H_3, which disrupts the formation of benzene. The chemical interaction between the nitrogen species and carbon species reduces the carbon availability for hydrocarbon growth and soot formation process. To isolate the effect of dilution, the NH_3-doped C_2H_4 flames were compared with those of N_2-doped flames at the same blend percentage. Results show that the chemistry effect of NH_3 on soot inhibition is significant, as evident from the net differences between the N_2-C_2H_4 and NH_3-C_2H_4 SVF profiles. The present work shows that NH_3 is effective in suppressing soot formation in hydrocarbon flames, but the chemical effects and reaction kinetics need to be further elucidated in detail to accurately describe the growth mechanism of soot.

Supplementary Materials: The following supporting information can be downloaded at: https://www.mdpi.com/article/10.3390/en15145209/s1, Values of K_e for NH_3-CH_4 flames.

Author Contributions: Conceptualization, C.T.C.; methodology, B.T.; validation; B.T. and C.T.C.; formal analysis, M.C. and B.T.; investigation, M.C. and B.T.; data curation, M.C.; writing-original draft preparation, C.T.C.; writing-review and editing, B.T., T.X. and M.C.; supervision and funding acquisition, C.T.C. All authors have read and agreed to the published version of the manuscript.

Funding: This research and APC was funded by Shanghai Jiao Tong University, grant number WF220428004.

Institutional Review Board Statement: Not applicable.

Informed Consent Statement: Not applicable.

Acknowledgments: The funding from the Shanghai Jiao Tong University (grant number: WF220428004) is gratefully acknowledged.

Conflicts of Interest: The authors declare no conflict of interest.

References

1. United Nation. COP26: Together for Our Planet. Available online: https://www.un.org/en/climatechange/cop26 (accessed on 4 February 2022).
2. Chong, C.T.; Fan, Y.V.; Lee, C.T.; Klemes, J.J. Post COVID-19 ENERGY sustainability and carbon emissions neutrality. *Energy* **2021**, *241*, 122801. [CrossRef]
3. Faye, O.; Szpunar, J.; Eduok, U. A critical review on the current technologies for the generation, storage, and transportation of hydrogen. *Int. J. Hydrogen Energy* **2022**, *47*, 13771–13802. [CrossRef]
4. Chiong, M.C.; Chong, C.T.; Ng, J.H.; Mashruk, S.; Chong, W.W.; Samiran, N.A.; Mong, G.R.; Valera-Medina, A. Advancements of combustion technologies in the ammonia-fuelled engines. *Energy Convers. Manag.* **2021**, *244*, 114460. [CrossRef]
5. Valera-Medina, A.; Xiao, H.; Owen-Jones, M.; David, W.I.F.; Bowen, P.J. Ammonia for power. *Prog. Energy Combust. Sci.* **2018**, *69*, 63–102. [CrossRef]
6. Elbaz, A.M.; Wang, S.; Guiberti, T.F.; Roberts, W.L. Review on the recent advances on ammonia combustion from the fundamentals to the applications. *Fuel Commun.* **2022**, *10*, 100053. [CrossRef]
7. Chai, W.S.; Bao, Y.; Jin, P.; Tang, G.; Zhou, L. A review on ammonia, ammonia-hydrogen and ammonia-methane fuels. *Renew. Sustain. Energy Rev.* **2021**, *147*, 111254. [CrossRef]
8. Wen, Y.; Zhang, S.; He, L.; Yang, S.; Wu, X.; Wu, Y. Characterizing start emissions of gasoline vehicles and the seasonal, diurnal and spatial variabilities in China. *Atmos. Environ.* **2021**, *245*, 118040. [CrossRef]
9. CAEP/8-IP/30. Committee on Aviation Environmental Protection (CAEP). Available online: https://web.mit.edu/aeroastro/partner/reports/caep8/caep8-nox-using-apmt.pdf (accessed on 5 April 2022).
10. IMO Sulphur Oxides (SOx) and Particulate Matter (PM)—Regulation 14. Available online: https://www.imo.org/en/OurWork/Environment/Pages/Sulphur-oxides-(SOx)-%E2%80%93-Regulation-14.aspx (accessed on 5 April 2022).
11. Li, Y.; Zhang, Y.; Yang, G.; Fuentes, A.; Han, D.; Huang, Z.; Lin, H. A comparative study on PAH characteristics of ethanol and ammonia as fuel additives in a premixed flame. *J. Energy Inst.* **2022**, *101*, 56–66. [CrossRef]
12. Ren, F.; Cheng, X.; Gao, Z.; Huang, Z.; Zhu, L. Effects of NH_3 addition on polycyclic aromatic hydrocarbon and soot formation in C2H4 co-flow diffusion flames. *Combust. Flame* **2022**, *241*, 111958. [CrossRef]
13. Montgomery, M.J.; Kwon, H.; Dreyer, J.A.H.; Xuan, Y.; McEnally, C.S.; Pfefferle, L.D. Effect of ammonia addition on suppressing soot formation in methane co-flow diffusion flames. *Proc. Combust. Inst.* **2021**, *38*, 2497–2505. [CrossRef]
14. Zhou, M.; Yan, F.; Ma, L.; Jiang, P.; Wang, Y.; Chung, S.H. Chemical speciation and soot measurements in laminar counterflow diffusion flames of ethylene and ammonia mixtures. *Fuel* **2022**, *308*, 122003. [CrossRef]
15. Cheng, X.; Li, Y.; Xu, Y.; Liu, Y.; Wang, B. Study of effects of ammonia addition on soot formation characteristics in n-heptane co-flow laminar diffusion flames. *Combust. Flame* **2022**, *235*, 111683. [CrossRef]
16. Boyette, W.R.; Steinmetz, S.A.; Guiberti, T.F.; Dunn, M.J.; Roberts, W.L.; Masri, A.R. Soot formation in turbulent flames of ethylene/hydrogen/ammonia. *Combust. Flame* **2021**, *226*, 315–324. [CrossRef]
17. Bennett, A.M.; Liu, P.; Li, Z.; Kharbatia, N.M.; Boyette, W.; Masri, A.R.; Roberts, W.L. Soot formation in laminar flames of ethylene/ammonia. *Combust. Flame* **2020**, *220*, 210–218. [CrossRef]
18. Li, Q.; Song, C.; Yan, Z.; Cao, X.; Wang, J.; Huang, Z. Effects of $NH_3/H_2/N_2$ addition on soot morphology and nanostructure in laminar co-flow ethylene diffusion flame. *Int. J. Hydrogen Energy* **2022**, *47*, 16321–16334. [CrossRef]
19. Michelsen, H.A.; Schulz, C.; Smallwood, G.J.; Will, S. Laser-induced incandescence: Particulate diagnostics for combustion, atmospheric, and industrial applications. *Prog. Energy Combust. Sci.* **2015**, *51*, 2–48. [CrossRef]
20. Tian, B. Laser Diagnostics of Soot in Hydrocarbon Diffusion Flames. Ph.D. Thesis, University of Cambridge, Cambridge, UK, 2016. Available online: https://www.repository.cam.ac.uk/handle/1810/309271 (accessed on 30 March 2022).
21. Tian, B.; Gao, Y.; Zhang, C.; Hochgreb, S. Soot measurement by combining continuous wave multi-pass extinction and laser-induced incandescence in diluted methane flames. *Combust. Flame* **2018**, *192*, 224–237. [CrossRef]
22. Tian, B.; Gao, Y.; Balusamy, S.; Hochgreb, S. High spatial resolution laser cavity extinction and laser induced incandescence in low soot producing flames. *Appl. Phys. B Lasers Opt.* **2015**, *120*, 469–487. [CrossRef]
23. Lambert, J.H. *Photometria Sive de Mensura et Gradibus Luminis, Colorum et Umbrae, 1760 (Photometry, or, On the Measure and Gradations of Light, Colors, and Shade, 1760)*; Nabu Press: Charleston, VA, USA, 2012.
24. Beer, A. Bestimmung der Absorption des rothen Lichts in farbigen Flüssigkeiten (Determination of the absorption of red light in colored liquids). *Ann. Phys. Chem.* **1852**, *86*, 78–88. [CrossRef]

25. Santoro, R.J.; Semerjian, H.G. Soot formation in diffusion flames: Flow rate, fuel species and temperature effects. *Symp. Combust.* **1985**, *20*, 997–1006. [CrossRef]
26. Puri, R.; Santoro, R.J.; Smyth, K.C. The oxidation of soot and carbon monoxide in hydrocarbon diffusion flames. *Combust. Flame* **1994**, *97*, 125–144. [CrossRef]
27. Santoro, R.J.; Semerjian, H.G.; Dobbins, R.A. Soot particle measurements in diffusion flames. *Combust. Flame* **1983**, *51*, 203–218. [CrossRef]
28. Moosmüller, H.; Arnott, W.P. Particle optics in the Rayleigh regime. *J. Air Waste Manag. Assoc.* **2009**, *59*, 1028–1031. [CrossRef] [PubMed]
29. Karataş, A.E.; Gülder, Ö.L. Soot formation in high pressure laminar diffusion flames. *Prog. Energy Combust. Sci.* **2012**, *38*, 818–845. [CrossRef]
30. Tian, B.; Zhang, C.; Gao, Y.; Hochgreb, S. Planar 2-colour time-resolved laser-induced incandescence measurements of soot in a diffusion flame. *Aerosol Sci. Technol.* **2017**, *51*, 1345–1353. [CrossRef]
31. Dasch, C.J. One-dimensional tomography: A comparison of Abel, onion-peeling, and filtered backprojection methods. *Appl. Opt.* **1992**, *31*, 1146–1152. [CrossRef]
32. Yon, J.; Lemaire, R.; Therssen, E.; Desgroux, P.; Coppalle, A.; Ren, K.F. Examination of wavelength dependent soot optical properties of diesel and diesel/rapeseed methyl ester mixture by extinction spectra analysis and LII measurements. *Appl. Phys. B* **2011**, *104*, 253–271. [CrossRef]
33. Dalzell, W.H.; Sarofim, A.F. Optical constants of soot and their application to heat-flux calculations. *J. Heat Transf.* **1969**, *91*, 100–104. [CrossRef]
34. D'Alessio, A.; Di Lorenzo, A.; Beretta, F.; Venitozzi, C. Optical and chemical investigations on fuel-rich methane-oxygen premixed flames at atmospheric pressure. *Symp. Combust.* **1973**, *14*, 941–953. [CrossRef]
35. Smyth, K.C.; Shaddix, C.R. The elusive history of m $\approx$ 1.57 $-$ 0.56i for the refractive index of soot. *Combust. Flame* **1996**, *107*, 314–320. [CrossRef]
36. Pochet, M.; Dias, V.; Moreaud, B.; Foucher, F.; Jeanmart, H.; Contino, F. Experimental and numerical study, under LTC conditions, of ammonia ignition delay with and without hydrogen addition. *Proc. Combust. Inst.* **2019**, *37*, 621–629. [CrossRef]
37. Wang, Y.; Chung, S.H. Soot formation in laminar counterflow flames. *Prog. Energy Combust. Sci.* **2019**, *74*, 152–238. [CrossRef]
38. Shao, C.; Campuzano, F.; Zhai, Y.; Wang, H.; Zhang, W.; Mani, S. Effects of ammonia addition on soot formation in ethylene laminar premixed flames. *Combust. Flame* **2022**, *235*, 111698. [CrossRef]
39. Steinmetz, S.A.; Ahmed, H.A.; Boyette, W.R.; Dunn, M.J.; Roberts, W.L.; Masri, A.R. Effects of ammonia and hydrogen on the sooting characteristics of laminar coflow flames of ethylene and methane. *Fuel* **2022**, *307*, 121914. [CrossRef]
40. Liu, Y.; Cheng, X.; Li, Y.; Qiu, L.; Wang, X.; Xu, Y. Effects of ammonia addition on soot formation in ethylene laminar diffusion flames. *Fuel* **2021**, *292*, 120416. [CrossRef]
41. Du, D.X.; Axelbaum, R.L.; Law, C.K. Soot formation in strained diffusion flames with gaseous additives. *Combust. Flame* **1995**, *102*, 11–20. [CrossRef]
42. Axelbalim, R.L.; Flower, W.L.; Law, C.K. Dilution and temperature effects of inert addition on soot formation in counterflow diffusion flames. *Combust. Sci. Technol.* **1988**, *61*, 51–73. [CrossRef]
43. Gülder, Ö.L.; Snelling, D.R. Influence of nitrogen dilution and flame temperature on soot formation in diffusion flames. *Combust. Flame* **1993**, *92*, 115–124. [CrossRef]
44. Gülder, Ö.L. Effects of oxygen on soot formation in methane, propane, and n-Butane diffusion flames. *Combust. Flame* **1995**, *101*, 302–310. [CrossRef]
45. Wang, Q.; Legros, G.; Bonnety, J.; Morin, C. Experimental characterization of the different nitrogen dilution effects on soot formation in ethylene diffusion flames. *Proc. Combust. Inst.* **2017**, *36*, 3227–3235. [CrossRef]
46. Gülder, Ö.L. Influence of sulfur dioxide on soot formation in diffusion flames. *Combust. Flame* **1993**, *92*, 410–418. [CrossRef]
47. Rossini, F.D.; Knowlton, J.W. Calorimetric determination of the heats of combustion of ethylene and propylene. *J. Res. NBS* **1937**, *19*, 249–262. [CrossRef]